JACS
JOURNAL OF THE AMERICAN CHEMICAL SOCIETY

Article

pubs.acs.org/JACS

# Elucidating Electrostatic Self-Assembly: Molecular Parameters as Key to Thermodynamics and Nanoparticle Shape

Giacomo Mariani,[†,‡] Daniel Moldenhauer,[†] Ralf Schweins,[‡] and Franziska Gröhn*[,†]

[†]Department of Chemistry and Pharmacy and Interdisciplinary Center for Molecular Materials (ICMM), Friedrich-Alexander-Universität Erlangen-Nürnberg, Egerlandstrasse 3, D-91058 Erlangen, Germany

[‡]Institut Laue-Langevin, DS/LSS, 71 Avenue des Martyrs, 38000 Grenoble, France

**ABSTRACT:** The rational design of supramolecular nanoparticles by self-assembly is a crucial field of research due to the wide applications and the possibility of control through external triggers. Understanding the shape-determining factors is the key for tailoring nanoparticles with desired properties. Here, we show how the thermodynamics of the interaction control the shape of the nanoparticle. We highlight the connection between the molecular structure of building blocks, the interaction strength, and the nanoassembly shape. Nanoparticles are prepared by electrostatic self-assembly of cationic polyelectrolyte dendrimers of different generations and oppositely charged multivalent organic dyes relying on the combination of electrostatic and $\pi-\pi$ interactions. Different building blocks have been used to vary interaction strength, geometric constraints, and charge ratio, providing insights into the assembly process. The nanoassembly structure has been characterized using atomic force microscopy, static light scattering, small angle neutron scattering, and UV−vis spectroscopy. We show that the isotropy/anisotropy of the nanoassemblies is related to the dye valency. Isothermal titration calorimetry has been used to investigate both dye−dye and dye−dendrimer interaction. The existence of a threshold value in entropy and enthalpy change separating isotropic and anisotropic shapes for both interactions has been demonstrated. The effects of the dye molecular structure on the interaction thermodynamics and therefore on the nanoparticle structure have been revealed using molecular modeling. The polar surface area of the dye molecule takes a key role in the dye self-interaction. This study opens the possibility for a priori shape determination knowing the building blocks structure and their interactions.

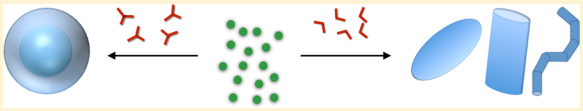

## INTRODUCTION

Self-assembly is an important route to organizing soft matter.[1−9] A variety of structures and functions in natural systems is realized by supramolecular assemblies, ranging from cell membranes to protein complexes for photosynthesis. Synthetic self-assembled structures with high potential are, for example, supramolecular polymers,[10−14] composite materials,[15−18] or carrier systems.[19−23] Great potential lies in the synthetic design for solar cells or drug delivery. In this framework, understanding the shape-determining factors is the key to a rational creation of target nanostructures. However, fundamental understanding of self-assembly often is limited. The architecture of the molecular building blocks has been demonstrated to be one of the key factors controlling the structure of the final nanoscale assemblies.[24−29] In the last years, the driving forces and the basic principles of the self-assembly process have been the topic of theoretical developments.[30−32] While the structure control in the self-assembly of amphiphilic systems is quite well known, different noncovalent interactions and their combinations have come into focus for nanostructure design more recently.[16,18,19,33] For example, we developed a new concept of electrostatic self-assembly for the formation of supramolecular nanoscale assemblies that show a well-defined size and exhibit a variety of shapes such as spheres, cylinders, and hollow spheres with narrow size distribution.[35−38] The process is based on the interconnection of macroions through "structural" multivalent organic counterions under secondary interaction effects such as $\pi-\pi$ stacking or geometric factors. Hence, the key point is a general combination of interactions, rather than relying on specific binding motifs. For instance, multivalent azo dye building blocks interconnect dendrimeric macroions into nanoparticles with sizes up to more than 100 nm.[35,39−42] Switchable nanoparticles that can respond to external triggers, such as pH or light, have been built,[7,35,41,42] and of particular potential are organic−inorganic hybrid assemblies where the polyelectrolyte enables the "communication" of an inorganic nanoparticle and the dye molecules.[43] Porphyrin−polyelectrolyte assemblies form a novel functional photocatalytic nanosystem for light energy conversion.[44]

Recently, the influence of the dendrimer size and the molecular structure of the dye building blocks on the resulting nanoparticle structures has been demonstrated.[45,46] A threshold in free energy below which no dendrimer interconnection takes place and a quantitative relation of the self-assembled nanoparticle size and the free energy of dye−dye and dye−dendrimer association became evident. The free energy of the assembly formation was shown to consist of an electrostatic contribution between dyes and dendrimers and a $\pi-\pi$ contribution between the dyes. Ultimately, a simple model has been developed to connect the free energy with the aggregation number.[47]

**Received:** November 3, 2015
**Published:** December 7, 2015





DOI: 10.1021/jacs.5b11497
J. Am. Chem. Soc. 2016, 138, 1280−1293

**Scheme 1. Azo Dyes and Dendrimer Building Blocks**

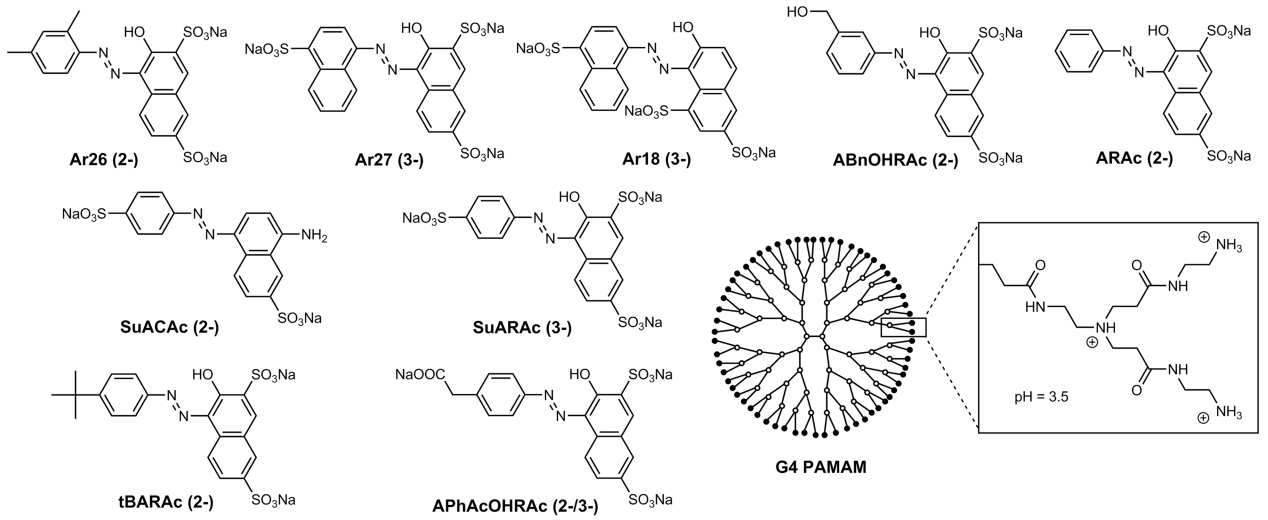


In contrast to the size tuning, the encoding of particle shape so far has not been understood, while this would open the possibility for shape control through building block selection.

At this point, for a thorough fundamental understanding on how electrostatic interaction, $\pi-\pi$ stacking, and geometric factors act together in the self-assembly on shape, a detailed structural characterization of the self-assembled nanoparticles is required focusing on the interplay of interactions with special attention to the role of the molecular building blocks. As a model system, we investigated electrostatically self-assembled nanoparticles from polyamidoamine (PAMAM) dendrimers and oppositely charged azo dyes (Scheme 1). The structure of the aggregates will be investigated as a function of the azo dye molecular structure, of the dendrimer generation (from 2 to 8), and of the component ratio. These parameters permit the modification of interaction strength, flexibility of the particles, geometric constraints, and charge compensation providing insights into the assembly process. An extended set of azo dyes, partially synthesized within this study, allows a systematic variation of the valency, the $\pi$-backbone, and the position of the charged groups. The nanoparticle structure has been characterized using atomic force microscopy (AFM), small angle neutron scattering (SANS), static light scattering (SLS), and UV−vis spectroscopy. Isothermal titration calorimetry (ITC) has been performed to study thermodynamics. Molecular modeling of the dye then permits one to connect the nanoscale structure and thermodynamics with the molecular dye properties. We present insight into the delicate balance of factors governing structure formation: it will be shown how the thermodynamics of the interaction between the building blocks controls not only the nanoassembly size but also their shape. Moreover, a relationship between the dye molecular properties and the interaction strength is established. This is a crucial step in creating a molecular toolbox allowing for directed self-assembly into tailor-made nanoparticles with desired shape and size by selecting appropriate building block combinations. To the best of our knowledge, this is the first time that a relationship of building block molecular properties, thermodynamics, and nanoscale shape is observed in electrostatic self-assembly.

## RESULTS AND DISCUSSION

This study comprises the structural characterization of the dye−dendrimer nanoparticles and the thermodynamic analysis of their formation including both the electrostatic interaction between dyes and dendrimers and the mutual $\pi-\pi$ interaction that occurs between the dyes, analyzing the changes in free energy, entropy, and enthalpy. The focus lies on understanding the structures formed, in particular, the assembly shape. Some of the dyes were already investigated in a previous study[50] (Ar26, tBARAc, ARAc, Ar27, Ar18, and SuARAc), while others have been synthesized within this study (APhAcOHRAc, ABnOHRAc, and SuACAc). To explore the role of electrostatic interaction, both di- (Ar26, ABnOHRAc, ARAc, tBARAc) and trivalent (APhAcOHRAc, Ar18, Ar27, SuARAc) dyes have been studied. In section 1 the structural characterization will be presented. It consists of AFM, SANS, and SLS to investigate the shape and size of the nanoparticles and UV−vis spectroscopy to study the $\pi-\pi$ stacking of the dye molecules. The loading ratio is defined as the molar ratio of dye sulfonate to dendrimer primary amino groups

$$l = \frac{c(-SO_3^-)}{c(-NH_2)} \quad (1)$$

In section 2 a detailed analysis of the dye−dye and dye−dendrimer interaction thermodynamics is presented where a key point is to draw a connection of the structural features on the nanoscale with the molecular level. In section 3, it is shown how the molecular electrostatic properties of the dye molecules control the dye−dye interaction and thereby the nanoparticle structure.

**1. Structural Characterization.** *AFM.* To obtain first structural information on the nanoaggregates, AFM measurements have been carried out. We investigated Ar26 with generation 4 and 8 dendrimers (G4 and G8). Results are displayed in Figure 1. The images show individual particles with different shapes for the two different samples. Ar26 and G4 dendrimers (Figure 1a) form ellipsoidal particles, while the shape is completely different when G8 is used (Figure 1b). In the latter case the nanoparticles are again elongated, but the aspect ratio is larger. These nanoaggregates are rod-like with a length of roughly 1 $\mu$m and a cross-section of 100 nm. In addition, these nanoparticles appear to be rather flexible in


DOI: 10.1021/jacs.5b11497
J. Am. Chem. Soc. 2016, 138, 1280−1293

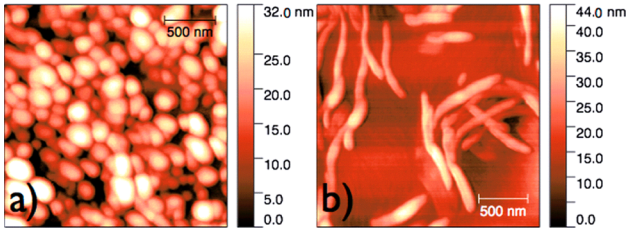


**Figure 1.** AFM images for (a) Ar26 + G4 at $l$ = 1.8 and (b) Ar26 + G8 at $l$ = 1.8.

comparison to the ones for Ar26 and G4. Therefore, we can conclude that different dendrimer generations result in different assembly shapes.

*SANS and SLS Measurements.* To gain insights into the nanoparticle shape and dimensions in solution we performed SANS experiments. Samples were prepared at pH 3.5 to provide complete protonation of the polyelectrolyte. Considering that a loading ratio of 2 corresponds to charge stoichiometry, we investigated loading ratios between 1 and 1.8, i.e., with excess of polyelectrolyte leading to well-defined and stable dye–dendrimer nanoparticles.[39] To better understand the shape of the nanoparticles, static light scattering measurements have been carried out. These measurements permit extending the $q$ range to lower $q$ values, covering the dimensions of the large nanoparticles.

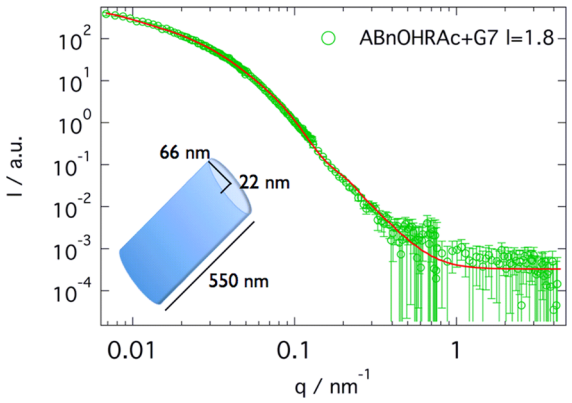


**Figure 2.** SANS results for ABnOHRAc + G7 at $l$ = 1.8.

The results for ABnOHRAc and G7 dendrimer are depicted in Figure 2. The SANS curve, at low $q$, clearly indicates the presence of nanoparticles in solution. From the $I(q_{min})$, one can conclude that the size is larger than 600 nm, which is 100 times larger than the building block size. To obtain the shape and the dimensions of the nanoaggregates, the curve has been fitted using structural models. In the case of ABnOHRAc and G7, the resulting nanoparticles are cylinders with elliptical cross-section with a length of 550 nm; the minor axis of the cross-section is 22 nm; the major one is 66 nm. Scattering curves for the most important samples including a series of varying loading ratios are shown in Figure 3. The corresponding shapes and dimensions are summarized in Tables 1 and 2: for different dyes and dendrimer generations, nanoparticles different in shape and dimension can be found. In the case of Ar26 and G4 dendrimer (Figure 3a) the nanoparticles are cylinders with elliptical cross-section; the length of the nanoparticles increases with the loading ratio, while the cross-section remains constant. From loading ratio 1.0 to 1.8 the length almost doubles, from 170 nm to 300 nm. This may be due to the incorporation of more dendrimer molecules; they are free at low loading ratios, while they connect to the nanoparticles at higher loading ratios. The polyelectrolyte molecules attach to the cylinders at the two ends, increasing their length and not changing the cross-section, thus modifying the particle aspect ratio. A different behavior can be found choosing APhAcOHRAc and G4 as building blocks (Figure 3c). Aggregates have a core–shell spherical shape and become smaller with loading ratio (from a total radius $R_{tot}$ = 87 nm to $R_{tot}$ = 46 nm). The fitting model describes a particle with a denser core and a less dense shell. Probably less dyes and dendrimers are incorporated in the shell, and hence, a less dense structure results. The behavior of ABnOHRAc and G7 (Figure 3d) is again different: at loading ratio 1.0 just single dendrimer molecules loaded with dye can be found. At loading ratios between 1.2 and 1.6, the molecular building blocks self-assemble into ellipsoids. At loading ratio 1.8 some of these ellipsoids aggregate together forming a larger elliptical cylinder. The same dye in combination with G8, as seen in Figure 3e, forms elliptical cylinders already at low loading ratio, and the cross-section remains unchanged while the length increases from 120 nm to 400 nm with the loading ratio. An interesting dependency results for Ar27 and G8 dendrimer (Figure 3f): at loading ratio 1.0 dendrimer dimers are observed, while at higher loading ratios two different structures coexist in solution: a small cylinder with the cross section of a single dendrimer molecule and a larger elliptical cylinder. The peculiarity of this system is that the cross-section of the elliptical cylinder increases with loading ratio, whereas in all other systems it remains constant.

In addition to the differences in the particle shape another behavior of the SANS curves results for all samples. At low loading ratio (below $l$ = 1.5), the curves clearly show two contributions: one at low $q$ and another around 0.7 nm$^{-1}$. The signal at low $q$ arises from the large nanoparticles formed by the interaction of dendrimers and dye molecules as discussed above, while the other can be attributed to small particles, which can be either individual dye-loaded dendrimers or small aggregates (size between 8 nm and 20 nm). The signal of the smaller particles is higher at loading ratio 1.0, where the excess of polyelectrolyte charges is maximal, and decreases continuously until loading ratio 1.5. At even higher loading ratio only the larger nanoassemblies are present in solution. Here the free polyelectrolyte molecules are loaded with sufficient dye to be all interconnected.

To summarize, the loading ratio is a crucial parameter in nanoparticle formation: it controls the dimensions of the nanoassemblies and the ratio between unassembled molecular building blocks and nanoparticles. In some cases it also has an effect on the shape of the self-assembled nanoparticles. With one exception, it plays no role on the cross-section of the aggregate. The shape and cross-section crucially depend on the building blocks, as will be discussed in the following.

To investigate the role of the dye structure and valency in the self-assembly, measurements have been made keeping the loading ratio and the dendrimer generation constant. Shape results are depicted in Scheme 2. Reading horizontally the line regarding G4, both spherical and elongated particles can be found, while in the case of G8 only elongated structures occur. For generation G4, three different structures can be observed: core–shell spheres, ellipsoids, and cylinders. Therefore, the dyes can be divided into two groups: the first forming isotropic aggregates (Ar18, Ar27, SuARAc, and APhAcOHRAc) and the second forming anisotropic particles (Ar26, ABnOHRAc,


DOI: 10.1021/jacs.5b11497
J. Am. Chem. Soc. 2016, 138, 1280–1293

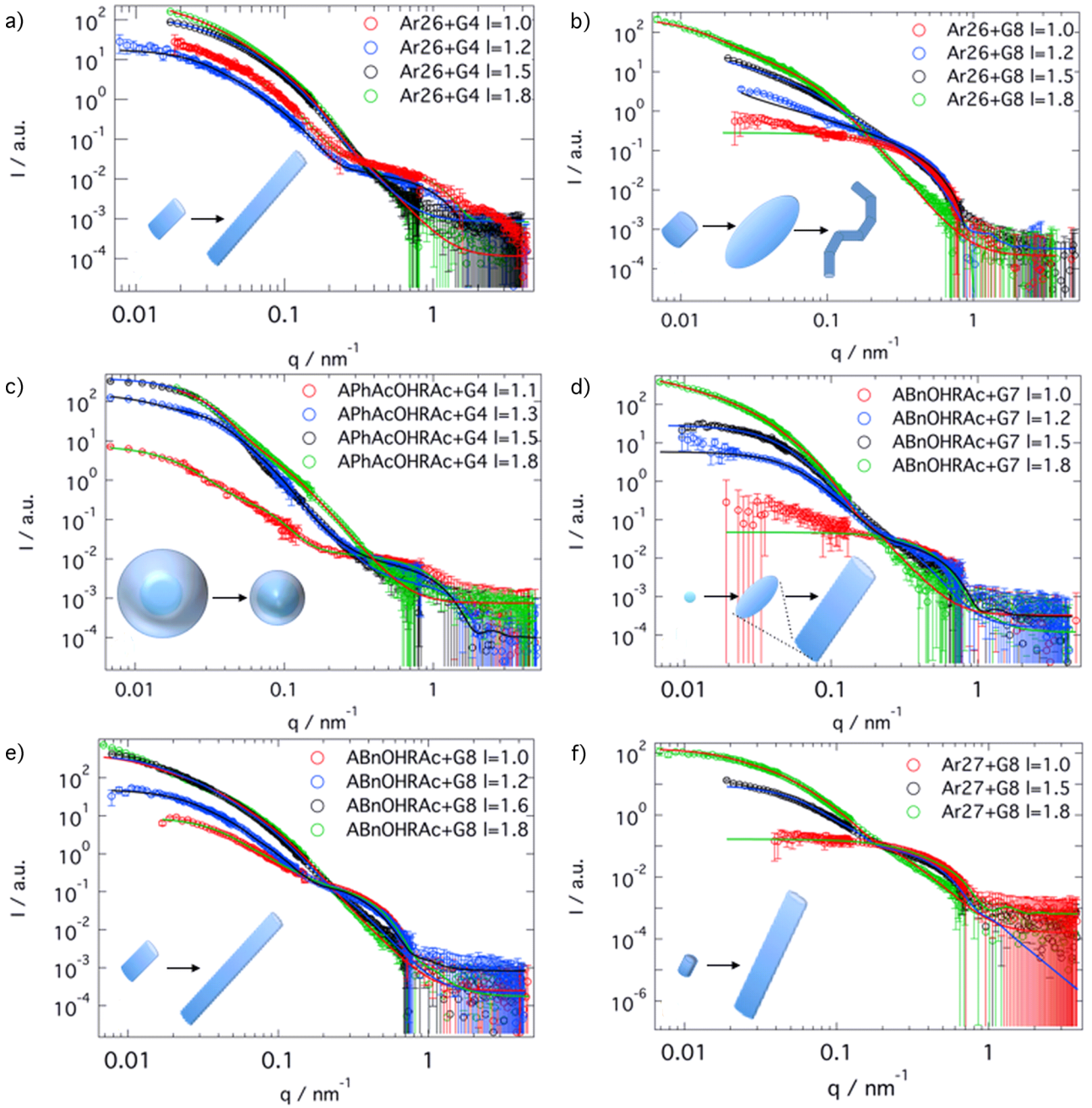


**Figure 3.** SANS results at different loading ratios for (a) Ar26 + G4, (b) Ar26 + G8, (c) APhAcOHRAc + G4, (d) ABnOHRAc + G7, (e) ABnOHRAc + G8, and (f) SuACAc + G8. Continuous lines represent the best fit. Results of the fits are summarized in Table 1.

SuACAc, ARAc, and tBARAc). For G4, among the dyes that form the same shape, the dimensions differ. In the case of spherical nanoparticles, the total radius $R_{tot}$ varies between 44 nm and 143 nm. tBARAc and SuACAc form ellipsoids. The axes of the nanoparticles made of tBARAc are 13 nm and 60 nm, while the ones of SuACAc are 47 nm and 120 nm. Ar26, ABnOHRAc, and ARAc form cylinders with elliptical cross-section. Despite a difference in length, Ar26 and ARAc show similar cross-section dimensions, which may be understood considering that more dendrimers attach to the end of the structure than to the side of the cylinder determining a preferred direction during the self-assembly process. ABnOHRAc instead forms longer cylinders, which become flexible. The choice of dye is crucial in targeting the dimensions of the nanoparticles.

To further investigate the influence of polyelectrolyte dimension and flexibility on the assembly structure, different dendrimer generations have been used. The shape results are again depicted in Scheme 2: this time the table should be read vertically. The SANS curves are reported in Figure 4. It is evident that the nanoparticle shape is strongly dependent on the dendrimer generation. In most cases (except of ABnOHRAc), a higher anisotropy is found for dendrimers of higher generation.

No isotropic nanoparticles can be found with G8 dendrimer. It can be concluded that the larger the polyelectrolyte building block is, i.e., the less flexible, the higher the anisotropy of the nanoassemblies. Even dyes that tend to form isotropic particles as a cause of their structural constraints are "forced" to build elongated structures by the G8 dendrimer. Looking in more detail at Ar26, the nanoparticles become more anisotropic as the


DOI: 10.1021/jacs.5b11497
J. Am. Chem. Soc. 2016, 138, 1280−1293

**Table 1. Geometric Parameters Resulting from the SANS Fits for Elongated Nanoparticles**

| | | | cross-section | | | | |
|---|---|---|---|---|---|---|---|
| system | $l$ | shape | $R_{min}$ (nm) | $R_{maj}$ (nm) | $L$ (nm) | $P$ (nm) | small particle |
| Ar26 + G2 | 1.8 | ellipsoid | 30 ± 1 | | 160 | | none |
| Ar26 + G4 | 1.0 | ellipt. cylinder | 12 ± 1 | 44 ± 4 | 170 ± 10 | | G4 |
| | 1.2 | ellipt. cylinder | 12 ± 1 | 46 ± 4 | 180 ± 10 | | G4 |
| | 1.5 | ellipt. cylinder | 11 ± 1 | 30 ± 3 | 185 ± 5 | | G4 |
| | 1.8 | ellipt. cylinder | 11 ± 1 | 44 ± 4 | 300 ± 10 | | none |
| Ar26 + G5 | 1.8 | cylinder | 35 ± 2 | | 220 ± 10 | | none |
| Ar26 + G7 | 1.0 | ellipt. cylinder | 35 ± 2 | 77 ± 5 | 175 ± 10 | | G7 |
| | 1.8 | flex. ellipt. cylinder | 22 ± 1 | 57 ± 3 | 870 ± 40 | 320 ± 20 | none |
| Ar26 + G8 | 1.0 | cylinder (= dimer) | 4 | | 19 ± 1 | | none |
| | 1.2 | cylinder | 4 | | 40 ± 2 | | none |
| | 1.4 | ellipsoid | 11 ± 1 | | 105 ± 5 | | cylinder as $l$ = 1.2 |
| | 1.5 | ellipsoid | 9 ± 1 | | 92 ± 5 | | cylinder as $l$ = 1.2 |
| | 1.7 | flex. ellipt. cylinder | 9 ± 1 | 31 ± 4 | 1400 ± 80 | 500 ± 20 | dimers |
| | 1.8 | flex. ellipt. cylinder | 10 ± 1 | 26 + 3 | 1400 ± 80 | 420 ± 20 | dimers |
| APhAcOHRAc + G8 | 1.0 | cylinder (= dimer) | 4 | | 20 ± 2 | | none |
| | 1.2 | ellipsoid | 19 ± 1 | | 130 ± 10 | | dimers |
| ABnOHRAc + G4 | 1.5 | flex. ellipt. cylinder | 7 ± 1 | 35 ± 5 | 710 ± 30 | 300 ± 20 | none |
| | 1.8 | flex. ellipt. cylinder | 7 ± 1 | 42 ± 6 | 2100 ± 100 | 140 ± 10 | none |
| ABnOHRAc + G5 | 1.0 | ellipsoid | 17 ± 1 | | 180 ± 10 | | G5 |
| ABnOHRAc + G7 | 1.0 | none | | | | | G7 |
| | 1.2 | ellipsoid | 14 ± 1 | | 86 ± 5 | | G7 |
| | 1.5 | ellipsoid | 18 ± 1 | | 120 ± 10 | | G7 |
| | 1.65 | ellipsoid | 19 ± 1 | | 130 ± 10 | | G7 |
| | 1.8 | ellipt. cylinder | 22 ± 1 | 66 ± 3 | 550 ± 20 | | none |
| APhAcOHRAc + G8 | 1.0 | cylinder (= dimer) | 4 | | 20 ± 2 | | none |
| | 1.2 | ellipsoid | 19 ± 1 | | 130 ± 10 | | dimers |
| ABnOHRAc + G8 | 1.0 | ellipt. cylinder | 12 ± 1 | 46 ± 4 | 120 ± 10 | | G8 |
| | 1.1 | ellipt. cylinder | 12 ± 1 | 41 ± 4 | 170 ± 10 | | G8 |
| | 1.2 | ellipt. cylinder | 17 ± 1 | 56 ± 3 | 200 ± 10 | | G8 |
| | 1.5 | ellipt. cylinder | 10 ± 1 | 37 ± 4 | 200 ± 10 | | G8 |
| | 1.6 | ellipt. cylinder | 14 ± 1 | 55 ± 4 | 340 ± 20 | | G8 |
| | 1.8 | ellipt. cylinder | 12 ± 1 | 48 ± 4 | 400 ± 20 | | none |
| Ar27 + G8 | 1.0 | cylinder (= dimer) | 4 | | 18 ± 1 | | none |
| | 1.5 | ellipt. cylinder | 13 ± 1 | 33 ± 3 | 200 ± 10 | | cylinder |
| | 1.8 | ellipt. cylinder | 28 ± 1 | 73 ± 3 | 260 ± 20 | | cylinder |
| SuARAc + G8 | 1.5 | flex. ellipt. cylinder | 11 ± 1 | 65 ± 7 | 210 ± 10 | 40 ± 3 | G8 |
| | 1.8 | flex. ellipt. cylinder | 8 ± 1 | 55 ± 7 | 2100 ± 90 | 40 ± 3 | none |
| SuACAc + G4 | 1.0 | ellipsoid | 11 ± 1 | | 120 ± 10 | | dimers |
| | 1.8 | ellipsoid | 47 ± 2 | | 240 ± 20 | | none |
| SuACAc + G8 | 1.0 | ellipsoid | 15 ± 1 | | 130 ± 10 | | dimers |
| | 1.5 | ellipsoid | 32 ± 2 | | 300 ± 20 | | none |
| | 1.8 | ellipsoid | 21 ± 1 | | 220 ± 20 | | none |
| tBARAc + G4 | 1.8 | ellipsoid | 13 ± 1 | | 120 ± 10 | | none |
| ARAc + G4 | 1.8 | ellipt. cylinder | 19 ± 1 | 57 ± 3 | 470 ± 20 | | none |
| ARAc + G8 | 1.8 | ellipsoid | 28 ± 2 | | 250 ± 10 | | none |

dendrimer generation increases. Ar26 and G2 form ellipsoids with one axis of 80 nm and the other of 30 nm. With G4 and G5, cylindrical particles are found, e.g., for G4 the length is 300 nm and the cross-section is elliptical with a minor axis of 11 nm and a major one of 44 nm. With G7 and G8, Ar26 forms flexible cylinders. For G7 the length is 870 nm, the persistence length is 320 nm, and minor and major axis are 22 nm and 57 nm. For Ar26 and G8 the length is 1.3 $\mu$m, the persistence length is 420 nm, the minor axis is 10 nm, and the major one is 26 nm. Interestingly, the cross-section aspect ratio is constant, while the overall aspect ratio doubles. Thus, by increasing the dendrimer size the self-assembled nanoparticles become larger and more elongated. A similar behavior can be found for APhAcOHRAc, changing the structure from spherical particles for G4 to ellipsoids for G8.

Hence, structural characterization reveals that the loading ratio controls the number of dendrimers forming the nanoparticles. Single dendrimers or dimers can coexist with larger nanoassemblies at low loading ratio, while at loading ratios above 1.5 all dendrimers are aggregated. For elongated nanoparticles, as the loading ratio increases, the length grows while the cross-section remains constant. The aspect ratio is therefore strongly related to the loading ratio. On the other hand, the shape of the assemblies is not related to the loading ratio in most cases. The assembly shape is caused by building block choice: different shapes originate from different dyes and



DOI: 10.1021/jacs.5b11497
J. Am. Chem. Soc. 2016, 138, 1280−1293

**Table 2. Geometric Parameters Resulting from the SANS Fits for Spherical Core–Shell Nanoparticles**

| system | $l$ | $R_{core}$ (nm) | $R_{tot}$ (nm) | small particle |
|---|---|---|---|---|
| APhAcOHRAc + G4 | 1.1 | 19 ± 1 | 87 ± 4 | G4 |
| | 1.3 | 29 ± 1 | 64 ± 3 | G4 |
| | 1.5 | 37 ± 2 | 52 ± 3 | G4 |
| | 1.8 | 28 ± 1 | 46 ± 2 | none |
| APhAcOHRAc + G5 | 1.0 | 2.9 | | none |
| | 1.8 | 61 ± 2 | 81 ± 3 | none |
| APhAcOHRAc + G7 | 1.0 | 59 ± 3 | 86 ± 4 | G4 |
| | 1.8 | 198 ± 10 | 273 ± 20 | none |
| Ar27 + G4 | 1.8 | 13 ± 1 | 44 ± 3 | none |
| Ar18 + G4 | 1.8 | 90 ± 3 | 143 ± 5 | none |
| SuARAc + G4 | 1.8 | 45 ± 2 | 64 ± 3 | none |

**Scheme 2. Nanoparticle Shapes Resulting from SANS as a Function of Dye Type and Dendrimer Generation**

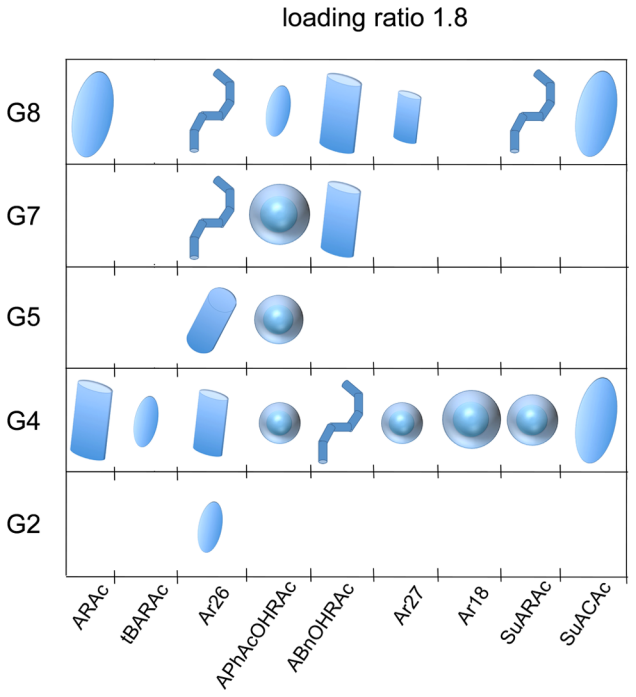


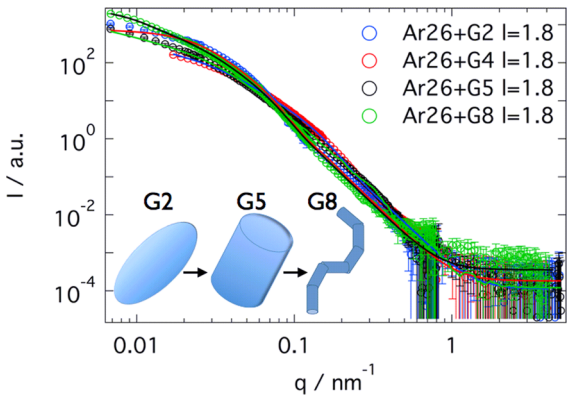


**Figure 4.** SANS curves of Ar26 and different dendrimer generations. Different shapes correspond to different generations.

different dendrimer generations. These two parameters together define the strength of dye–dendrimer and dye–dye interaction, stemming from differences in dye valency, geometry, dimensions, number of interacting points, and dendrimer flexibility. Higher dendrimer generations promote the formation of anisotropic nanoparticles as well as larger particle sizes.

*UV–vis Spectroscopy.* UV–vis results for different dyes and two dendrimer generations (G4 and G8) are depicted in Figure 5. The binding of dyes to dendrimers due to ionic interaction induces the spatial proximity of the dye molecules, and thereby dyes can mutually interact and form $\pi$-stacks.[38,39,47,48] This causes the splitting of the first excited state of the monomer and can be described applying exciton theory.[49−53] From this, two geometric parameters can be extracted: the intermolecular dye–dye distance $R$ and the twist angle $\beta$ between two dyes molecules.[54] The fitting results are given in Figure 5 and, for loading ratio $l$ = 1.8 in Table 3. It is worth noting how the twist angle is related to the nanoparticle shape. For G4 dendrimer, for all systems forming isotropic structures the angle is around 37–38°, while for anisotropic structures it is higher than 40°. Moreover, with G8 (i.e., where all systems form elongated structures) only angles larger than 40° are observed. The twist angle versus the loading ratio is depicted in Figure 6. Taking into account the angular behavior in the case of G4, assemblies with different shape show a different variation of the twist angle. For spherical particles the angle remains constant (variation of less than 3°), while for elongated particles it changes by 15°. For G8, instead, the changes are larger than 25°. ABnOHRAc differs: it forms elongated structures with both G4 and G8, but the angle is independent of loading ratio and dendrimer generation. As shown from SANS measurements, it must be kept in mind that single dendrimers loaded with dyes can be found at loading ratios lower than 1.5. The presence of this second species can influence the UV–vis measurements and consequently the angle. The intermolecular dye distance $R$ appears not to be connected to the shape of the nanoparticle but only depends on the dye itself. There appears to be a fixed range of dye–dye distances from 0.65 to 0.80 nm for all dyes.[55] Further discussions of the structural parameters obtained from the UV–vis measurements will be presented in the next section in context with the thermodynamics results. In conclusion, all dyes with twist angles larger than 40° form anisotropic nanoparticles, whereas the dyes that form isotropic aggregates have a constant angle of about 38°.

**2. Thermodynamics.** Previously, isothermal titration calorimetry has led to an attraction–repulsion model allowing the understanding of the finite assembly size. It has been demonstrated that the assembly process is governed by the mutual dye–dye interaction. No relation of thermodynamics and nanoscale shape of the self-assembled particles exists so far.

Herein, we extend the ITC measurements to a larger set of dyes and dendrimer generations while simultaneously elucidating how the thermodynamics of the interaction encodes the shape of the nanoparticles. For this purpose, both dye dilution experiments and dendrimer into dye titrations were performed to investigate the dye self-aggregation and the dye–dendrimer interaction, respectively. In the following, first, the results on dye–dye interaction and, second, those on dye–dendrimer interaction will be presented, relating all of them to the shape of the nanoparticles.

ITC raw data and their analysis are shown in Figure 7. The raw heat traces of the titration experiments are depicted in the upper plot. For the dilution experiments (Figure 7a and 7b), the lower plot shows the integrated heat for each injection versus the dye concentration in the titration cell. For the dye–dendrimer experiments (Figure 7c and 7d), again the lower plot


DOI: 10.1021/jacs.5b11497
J. Am. Chem. Soc. 2016, 138, 1280–1293

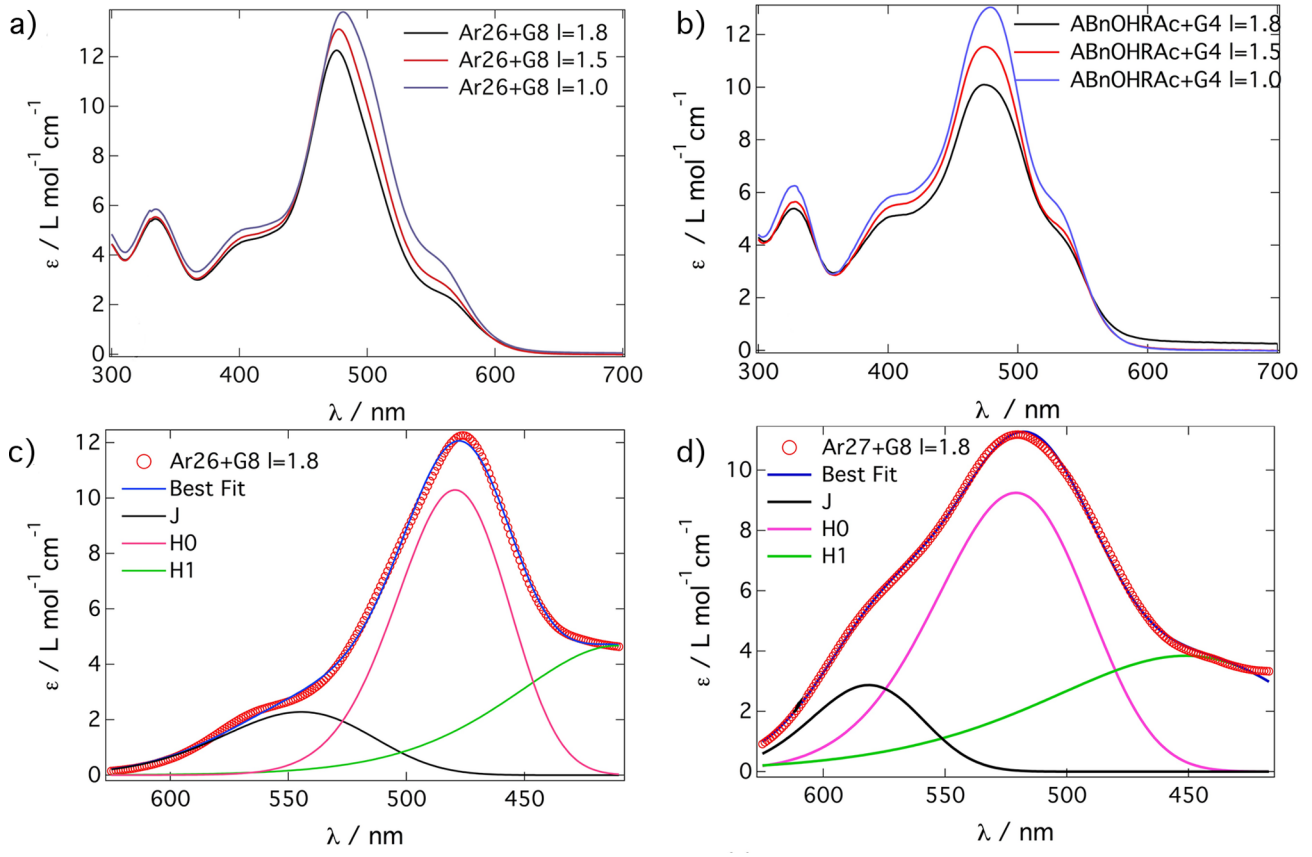


**Figure 5.** UV−vis spectroscopy. (a) Spectra for Ar26 + G8 at three loading ratios. (b) Spectra for ABnOHRAc + G4 at three loading ratios. (c and d) Exction theory applied to Ar26 + G8 and Ar27 + G8.

**Table 3. Analysis of Mutual Dye Geometry According to Exciton Theory at Loading Ratio $l$ = 1.8**

| system | $R$ (nm) | $\beta$ (deg) |
|---|---|---|
| Ar26 + G4 | 0.75 ± 0.03 | 55 ± 1 |
| tBARAc + G4 | 0.65 ± 0.03 | 43 ± 1 |
| ABnOHRAc+ G4 | 0.71 ± 0.03 | 38 ± 1 |
| APhAcOHRAc + G4 | 0.74 ± 0.03 | 38 ± 1 |
| SuARAc + G4 | 0.75 ± 0.03 | 38 ± 1 |
| Ar27 + G4 | 0.65 ± 0.04 | 37 ± 1 |
| Ar26 + G8 | 0.68 ± 0.04 | 51 ± 1 |
| tBARAc + G8 | 0.68 ± 0.03 | 67 ± 1 |
| ABnOHRAc + G8 | 0.73 ± 0.03 | 39 ± 1 |
| APhAcOHRAc + G8 | 0.75 ± 0.03 | 41 ± 1 |
| SuARAc + G8 | 0.75 ± 0.03 | 45 ± 1 |
| Ar27 + G8 | 0.78 ± 0.02 | 46 ± 1 |

shows the integrated heat normalized per mole of injectant versus molar ratio of dendrimer to dye in the titration cell. The ITC curves can then be extrapolated to zero molar ratio to obtain the enthalpy of association, or they can be fitted with a one-site model. The two approaches yield the same results, and the one-site model will be applied in the following. It yields the equilibrium aggregation constant $K$ and consequently the Gibbs free energy change of the association $\Delta G$,[56,57] and together with the enthalpy change $\Delta H$ it leads to the entropy change $\Delta S$:

$$\Delta G = -RT \ln K \quad (2)$$

$$\Delta G = \Delta H - T\Delta S \quad (3)$$

Results for the dye dilution are reported in Table 4. Values between $\Delta H_{\text{dye−dye}} = -30$ kJ mol$^{-1}$ and $\Delta H_{\text{dye−dye}} = -8$ kJ mol$^{-1}$ have been found, while the entropy change is between $T\Delta S_{\text{dye−dye}} = -21$ kJ mol$^{-1}$ and $T\Delta S_{\text{dye−dye}} = -4$ kJ mol$^{-1}$. The trivalent dyes (Ar18, Ar27, and SuARAc) show a higher $\Delta H_{\text{dye−dye}}$ than the divalent ones. Their values vary between $\Delta H_{\text{dye−dye}} = -8$ kJ mol$^{-1}$ and $\Delta H_{\text{dye−dye}} = -20$ kJ mol$^{-1}$, while the divalent ones have enthalpies lower than $\Delta H_{\text{dye−dye}} = -20$ kJ mol$^{-1}$. APhAcOHRAc with $\Delta H_{\text{dye−dye}} = -20.2$ kJ mol$^{-1}$ lies between the trivalent dyes and the divalent ones. This is due to its carboxylic acid group with a p$K_a$ of 4.1. At pH 3.5 the dye is to 20% in the trivalent and to 80% in the divalent state. This may be used to tune its valency by regulating the pH, opening new possibilities in the control of the nanoparticle shape.

Considering the $\Delta H_{\text{dye−dye}}$ in conjunction with the shape of the nanoparticles as measured by SANS (Figure 8), a threshold value clearly appears around $\Delta H_{\text{dye−dye}} = -21$ kJ mol$^{-1}$: below that self-assembly into spherical nanoparticles occurs, above it self-assembly into elongated structures occurs. Moreover, this value separates tri- and divalent dyes, because trivalent dyes form isotropic assemblies while divalent ones form anisotropic assemblies. Therefore, the valency of the organic dye ions is a crucial parameter in controlling the shape of the self-assembled nanoparticles. Due to the additional charge, trivalent dyes bind to a greater extent to protonated amino groups, and this may restrict the geometric conformations available. In the case of APhAcOHRAc, 20% of trivalent state is sufficient to prevent the formation of elongated particles and forces the nanoparticles to be spherical. Furthermore, the trivalent dye molecules likely require more expressed configuration changes of the dendrimer



DOI: 10.1021/jacs.5b11497
J. Am. Chem. Soc. 2016, 138, 1280−1293

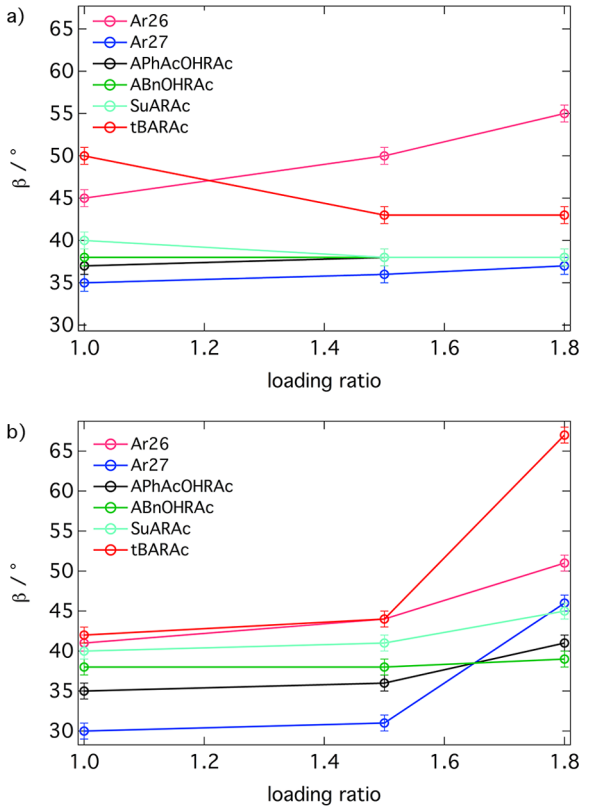


**Figure 6.** Geometric results from the exciton analysis: twist angle in dependence on different loading ratios (a) for G4 dendrimer and (b) for G8 dendrimer.

to realize a high number of ion pairs of dye sulfonate and dendrimer ammonium groups, and steric hindrance plays a role. This is confirmed when the ratio of the number of dyes bound to one dendrimer molecule to the maximum number of dye molecules that can bind to the dendrimer is considered: for divalent dyes this varies between 0.94 and 0.98, while for trivalent dyes it is between 0.90 and 0.93 only. Moreover, the divalent dyes have a lower value for the enthalpy than the trivalent dyes. This means that elongated particles can be formed only when the dye−dye interaction is strong enough and, in more detail, that only the dyes with a strong $\pi-\pi$ interaction can form anisotropic nanoparticles. This can be understood considering that the dye−dye interaction is mainly anisotropic and thus may induce a preferred growth direction to the assemblies.

Next, it is of interest to consider the free energy change $\Delta G_{\text{dye-dye}}$. Trivalent dyes show values between $\Delta G_{\text{dye-dye}} = -15$ kJ mol$^{-1}$ and $\Delta G_{\text{dye-dye}} = 13$ kJ mol$^{-1}$, while the divalent ones have values lower than $\Delta G_{\text{dye-dye}} = -15$ kJ mol$^{-1}$. Again, APhAcOHRAc with $\Delta G_{\text{dye-dye}} = -16$ kJ mol$^{-1}$ has a value that lies between the two kinds of counterions. The threshold also can be observed in dye−dye entropy $T\Delta S_{\text{dye-dye}}$. The fact that the threshold is evident in all thermodynamic dye−dye parameters but most expressed in $\Delta H_{\text{dye-dye}}$ reflects the fact that the dye−dye interaction is enthalpy dominated. It is predominantly caused by $\pi-\pi$ overlap energy rather than by a hydrophobic effect entropic in nature. Hence, it is clearly evident that the dye−dye interaction is crucial, not only for extended dendrimer interconnection but also for encoding the aggregate shape. For the first time it is possible to predict the structure of the nanoparticles formed by dendrimers and dyes by knowing the strength of the dye−dye interaction. This is a key step in the definition of a molecular toolbox that allows for a targeted structure design in terms of assembly size and shape.

Furthermore, the dye−dendrimer interaction has been investigated. For these studies G4 dendrimer has been used as polyelectrolyte, as reported in Table 5. In particular, trivalent dyes yielding spherical aggregates have lower values for both enthalpy and entropy change. Figure 9 displays the interplay of enthalpy and entropy. Here, the three trivalent dyes lie in the left corner of the graph. The difference in enthalpy and entropy change is approximately 10 kJ mol$^{-1}$. Spherical and elongated structures are again separated in $\Delta H_{\text{dye-den}}$ and $T\Delta S_{\text{dye-den}}$ as was found for the dye−dye interaction. For APhAcOHRAc, which is a mixture of di- and trivalent dyes at pH 3.5, $\Delta H_{\text{dye-den}}$ and $T\Delta S_{\text{dye-den}}$ lie between the two regions but closer to the values of the divalent dyes. This might be expected because the divalent configuration is predominant. In particular, $\Delta H_{\text{dye-den}}$ for APhAcOHRAc is almost identical to that of the divalent dye tBARAc, resulting in a less defined threshold between elongated and spherical aggregates. Despite the differences in enthalpy and entropy, the so-called entropy−enthalpy compensation can be

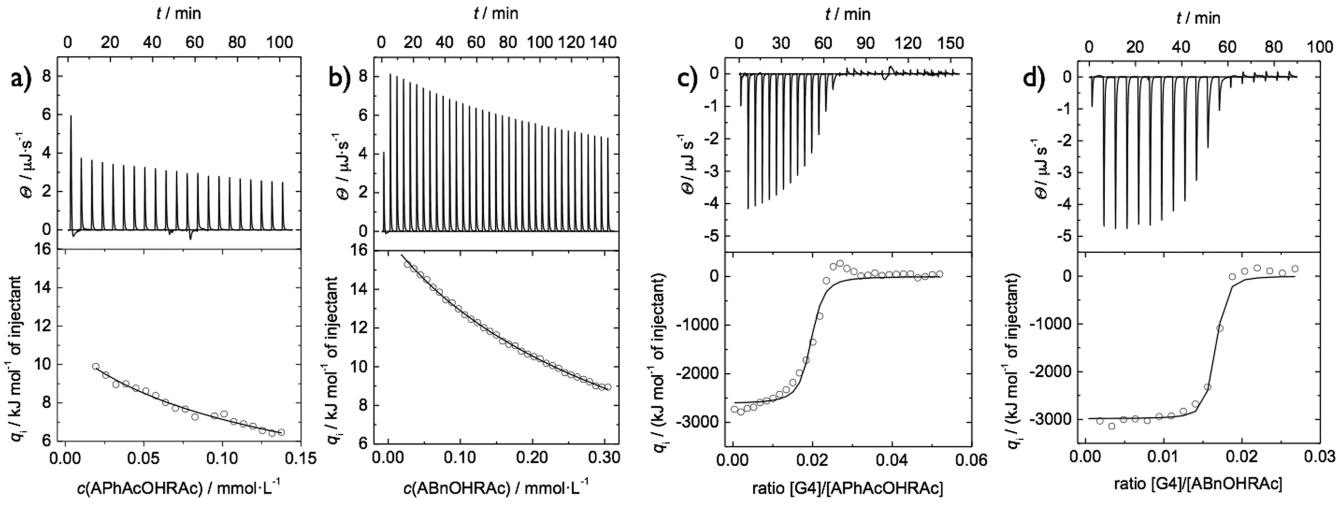


**Figure 7.** Isothermal titration calorimetry for (a) dilution of APhAcOHRAc, (b) dilution of ABnOHRAc, (c) titration of G4 dendrimer into APhAcOHRAc, and (d) titration of G4 dendrimer into ABnOHRAc, all in formic acid buffer (pH = 4).



DOI: 10.1021/jacs.5b11497
J. Am. Chem. Soc. 2016, 138, 1280−1293

**Table 4. Thermodynamic Data for the Dye−Dye Interaction Resulting from ITC**

| dye | charge | $\Delta H_{dye-dye}$ (kJ mol$^{-1}$) | $K_{dye-dye}$ (L mol$^{-1}$) | $\Delta G_{dye-dye}$ (kJ mol$^{-1}$) | $T\Delta S_{dye-dye}$ (kJ mol$^{-1}$) |
|---|---|---|---|---|---|
| SuACAc | 2− | −29.1 | $1.1 \times 10^3$ | −17.4 | −11.6 |
| Ar26 | 2− | −29.0 | $2.9 \times 10^3$ | −19.8 | −9.2 |
| tBARAc | 2− | −25.4 | $6.3 \times 10^2$ | −16.0 | −9.4 |
| ABnOHRAc | 2− | −24.3 | $5.0 \times 10^2$ | −15.4 | −8.9 |
| APhAcOHRAc | 2− | −20.2 | $5.8 \times 10^2$ | −15.8 | −4.4 |
| Ar27 | 3− | −20.0 | $1.3 \times 10^2$ | −12.0 | −8.0 |
| SuARAc | 3− | −8.2 | $5.6 \times 10^{-3}$ | 12.9 | −21.1 |

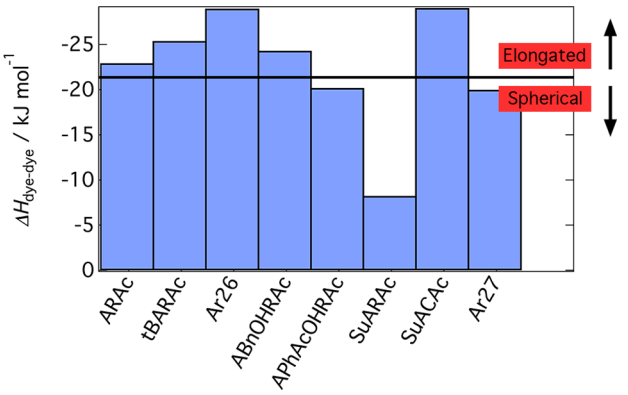


**Figure 8.** Enthalpy variation measured for dye−dye interaction. A threshold value at $\Delta H_{dye-dye} = -21$ kJ mol$^{-1}$ separates elongated and spherical structures.

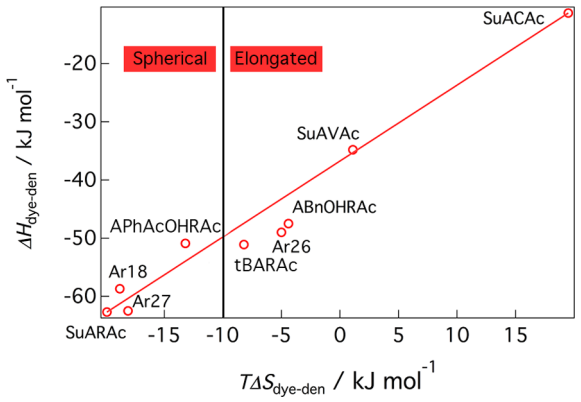


**Figure 9.** Enthalpy−entropy relation for dye−dendrimer interaction.

seen in Figure 9.[46] In the present study more dyes have been investigated and a more precise fit can be presented, which yields a slope of 1.3. This means that the interplay of enthalpy and entropy changes the free energy to some extent. A clear separation is found if the dye−dendrimer entropy exchange is taken into account: the trivalent dyes and APhAcOHRAc are the ones with the lowest entropy. A threshold value between anisotropic and isotropic structures can be identified for the interaction around $T\Delta S_{dye-dendrimer} = -10$ kJ mol$^{-1}$.

It is now of great interest to connect the results from UV−vis to the thermodynamic interaction parameters. First, the twist angle as a function of the dye−dye interaction enthalpy $\Delta H_{dye-dye}$ can be analyzed. As reported in Figure 10 for G4 dendrimer, the angle is constant for the isotropic structures, while it changes for elongated particles. Thus, it is evident that the twist angle is related to the nanoscale structure and, therefore, to the strength of the dye−dye interaction. For the dyes forming spherical particles the angle varies less than 1°, while for the others it changes by approximately 16°. Interestingly, the angle for the divalent dyes appears to vary linearly with $\Delta H_{dye-dye}$. Therefore, it can be concluded that a certain interaction strength is required to obtain elongated

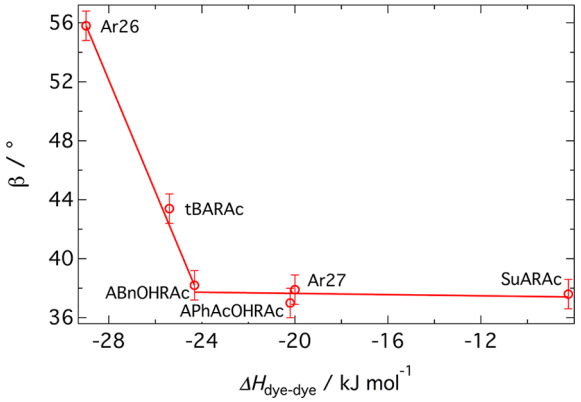


**Figure 10.** Twist angle in dependence on $\Delta H_{dye-dye}$. For trivalent dyes it is constant, while for divalent ones it changes linearly with $\Delta H_{dye-dye}$.

structures; this increased strength acts on the angle between the dye molecules, yielding a more tilted configuration. Remarkably, the angle of ABnOHRAc, a dye forming elongated structures, is equal to the value measured for the trivalent dyes. It is therefore equal to the twist angle of the dyes in the spherical structure.

**Table 5. Thermodynamic Data for the Dye−Dendrimer G4 Interaction Resulting from ITC**

| dye | charge | $\Delta H_{dye-den}$ (kJ (mol dye)$^{-1}$) | $N_{dye\ per\ G4}$ | $K_{dye-den}$ (L mol$^{-1}$) | $\Delta G_{dye-den}$ (kJ (mol dye)$^{-1}$) | $T\Delta S_{dye-den}$ (kJ (mol dye)$^{-1}$) |
|---|---|---|---|---|---|---|
| SuACAc | 1− | −11.3 | 206 | $2.6 \times 10^5$ | −30.9 | 19.5 |
| Ar26 | 2− | −49.0 | 62 | $5.0 \times 10^7$ | −44.0 | −5.0 |
| ABnOHRAc | 2− | −47.5 | 63 | $3.6 \times 10^7$ | −43.1 | −4.4 |
| tBARAc | 2− | −51.1 | 59 | $3.0 \times 10^7$ | −42.9 | −8.2 |
| APhAcOHRAc | 2− | −50.9 | 52 | $3.9 \times 10^6$ | −37.6 | −13.2 |
| Ar18 | 3− | −58.7 | 38 | $1.0 \times 10^7$ | −39.9 | −18.8 |
| Ar27 | 3− | −62.5 | 39 | $6.0 \times 10^7$ | −44.4 | −18.1 |
| SuARAc | 3− | −62.7 | 38 | $3.2 \times 10^7$ | −42.8 | −19.9 |



DOI: 10.1021/jacs.5b11497
J. Am. Chem. Soc. 2016, 138, 1280−1293

Scheme 3. Electrostatic Potential at the Molecular Surface for the Dye Molecules: Each Top View (left) and Front View (right)

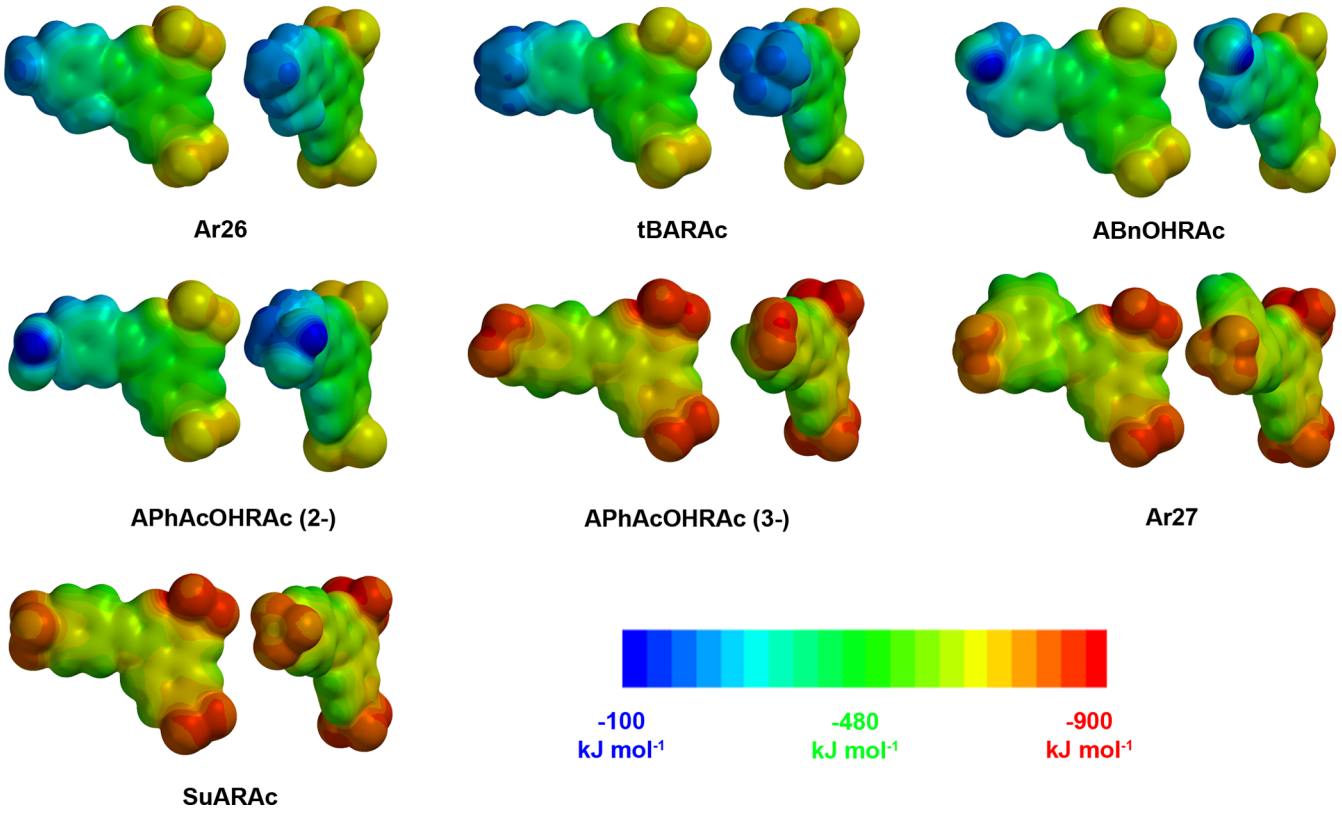


This means that the structural transition between isotropic and anisotropic nanoparticles is continuous and no steps occur.

If then the interaction with G8 is taken into account, no structural transition is observed and only anisotropic structures are formed. This may be understood considering that G8 dendrimer is larger, more dense, and less flexible than G4; therefore, the possibility for the dye to direct the stacking and exhibit varying twist angles is more limited as compared to the interaction with G4 dendrimer.

**3. Molecular Building Block Parameters.** The strong relationship of dye−dye interaction strength, dye twist angle, and nanoscale structure represents new insight into the concept of electrostatic self-assembly. It is highly desirable, yet challenging, to understand it more deeply. Evidently, thermodynamics encodes the nanoscale supramolecular structure, while the molecular structure of the building blocks encodes thermodynamics. The challenging question remaining at this point is which molecular parameter, property, or combination thereof is the basis.

From a theoretical point of view, the $\pi-\pi$ interaction of aromatic systems has been mainly investigated considering polarized $\pi$-systems and electrostatic arguments, for example, the interaction of two quadrupole moments.[58] Only in the last years, the role of the substituents in $\pi-\pi$-interaction has been in focus, for example, in the case of fluorine-substituted benzene derivatives.[59−63] Studying the strengths of the stacking interaction in the case of meta- and para-substituted *N*-benzyl-2-(2-fluorophenyl)pyridinium bromides, the electrostatic interaction of the polarized atoms associated with more polarized substituents was shown to dominate the geometries and energetics of stacked systems.[64]

To elucidate the role of the dye molecular structure on the dye−dye interaction and consequently on the self-assembly, we here consider the dipole moment $\mu$, the polarizability $\alpha$, and the polar surface area *PSA* of the molecule. The *PSA* is the sum of the areas of the van der Waals surfaces of the polar atoms in a molecule, which has been demonstrated to be crucial to predict drug transport properties.[65,66] The dipole moment has been related to the free energy of the dimerization for merocyanine dyes.[67]

First, the electrostatic potential at the molecular surface needs to be considered. This is the three-dimensional charge distribution of the molecule and can be used to understand its interaction with other molecules. A visual representation of the electrostatic potential is given in Scheme 3. The dye molecules can be divided in two parts: the R-Acid part with a naphthalene core and two sulfonate charges, chemically identical for all of them, and the "left part" with a benzene ring and a substituent (except Ar27 that possesses a naphthalene ring). The differences in electrostatic potential between the dye molecules originate from this "left part": depending on the substituent the aromatic system ($R_{left\text{-}part}-N{=}N-R_{R\text{-}Acid}$) changes the electrostatic potential. In a first approximation the electrostatic potential can be related to the dye−dye interaction strength: the $\Delta H_{dye-dye}$ decreases as the electrostatic potential in the "left part" becomes more negative. In particular, this molecular property can be the reason why the ABnOHRAc twist angle is remarkably lower than the one of the other divalent dyes. The differences in the electrostatic potential are due to the different substituents. If a charged substituent is present, i.e., for the trivalent dyes, the entire aromatic system shows a more negative electrostatic potential being equivalent to an electron-richer system. With a noncharged substituent, both the left and the R-acid part are less negative, i.e., a bit electron poorer. Further, the electrostatic potential of the noncharged substituent is less negative than the rest of the molecule. Fundamentally, the


DOI: 10.1021/jacs.5b11497
J. Am. Chem. Soc. 2016, 138, 1280−1293

potential is defined by the atoms and their electronegativity, thus also describing the bond character. For example, the methyl and *tert*-butyl groups in Ar26 and tBARAC, respectively, incorporate a high amount of hydrogen and therefore show a less negative potential (absence of electron density). In the carboxymethyl group of APhAcOHRAc the oxygen with its high electronegativity withdraws electron density and thus shows a more negative potential. At the same time this induces a less negative potential at the carboxylic acid hydrogen, revealing its protic character.

Further, it is of interest to establish connections between the dipole moment, the polarizability, and the *PSA* with the assembly behavior, all molecular properties based on the electrostatic potential. The parameters for the dyes used herein are reported in Table 6. The trivalent dyes' dipole moment is

**Table 6. Electrostatic Parameters for the Different Dyes**

| dye (charge) | $\mu$ (D) | $\alpha$ (Å$^3$) | PSA (Å$^2$) | $\Delta H_{dye-dye}$ (kJ mol$^{-1}$) | $\beta$ (deg) |
|---|---|---|---|---|---|
| Ar26 (2−) | 24.6 | 71.0 | 144.1 | −29.0 | 55 |
| tBARAc (2−) | 30.9 | 73.9 | 145.6 | −25.4 | 43 |
| ABnOHRAc (2−) | 23.3 | 70.1 | 165.3 | −24.3 | 38 |
| APhAcOHRAc (2−) | 29.2 | 71.8 | 180.4 | −20.2 | 38 |
| APhAcOHRAc (3−) | 3.8 | 71.6 | 175.1 | −20.2 | 38 |
| Ar27 (3−) | 10.2 | 75.4 | 201.2 | −20.0 | 37 |
| SuARAc (3−) | 2.5 | 71.0 | 204.9 | −8.2 | 38 |

lower than that of the divalent ones: the dipole moment of the divalent APhAcOHRAc is $\mu$ = 29.2 D, while the trivalent configuration has a $\mu$ = 3.8 D. On the other hand, polarizability is very similar for all molecules: the highest polarizabilities are observed for one divalent (tBARAc) and one trivalent dye (Ar27) with $\alpha$ = 73.9 and 75.4 Å$^3$, respectively. Instead, the *PSA* is different for each dye, and trivalent dyes have higher values compared to the divalent ones.

It is then of interest to observe how the dipole moment and the *PSA*, i.e., the polar surface area of the molecule, vary as a function of the dye−dye interaction strength (i.e., $\Delta H_{dye-dye}$) and if they can be connected to the nanoparticle shape and the dye twist angle. It is evident that the dyes that interact strongly (divalent ones) have the highest dipole moment. The *PSA*, as described in Figure 11a, increases as the $\Delta H_{dye-dye}$ increases, and the dyes with the weaker interaction have larger *PSAs*. Since the PSA results from the area of the polar groups in the molecule and, in particular, takes the subsituents into account more explicitly than the polarizability that refers to the molecule as a whole, the PSA can be well related to the dye self-interaction. Hence, the PSA encodes the mutual dye interaction and, in particular, the dye−dye electrostatic repulsion. The lower the *PSA* the better the dye molecules can interact with each other. This explains the relationship of *PSA* and $\Delta H_{dye-dye}$: $\Delta H_{dye-dye}$ is higher (i.e., strong dye−dye interaction) for particles with low *PSA*. In detail, Ar26 is the dye with the lowest *PSA* and the highest $\Delta H_{dye-dye}$. The trivalent dyes instead show higher *PSA* values, resulting in a less strong interaction. This effect is opposite to electron-withdrawing and -donating substituents influencing the $\pi-\pi$ overlap interaction as such[63,68,69] and electron-rich substituents enhancing $\pi-\pi$ interaction likely through subsituent−$\pi$ interaction[63,69,70] and in difference to steric subsituent effects influencing $\pi-\pi$ intercation strength, for example, by modifying the planarity of the $\pi$-system.[68] For sets

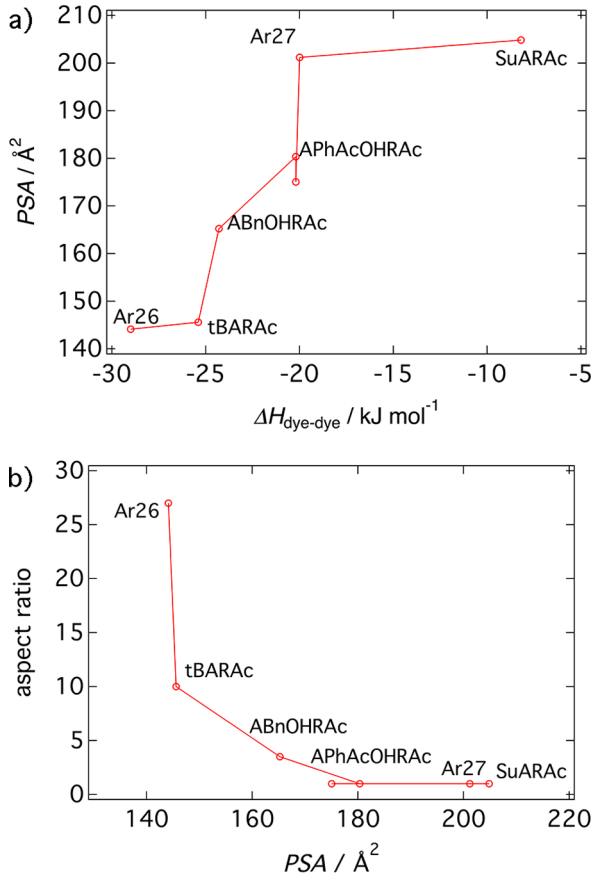


**Figure 11.** (a) Polar surface area as a function of $\Delta H_{dye-dye}$. (b) Nanoparticle aspect ratio as a function of *PSA*.

of building blocks with (almost) unchanged $\pi$-systems and strongly polar (e.g., negatively charged) subsituents, evidently, the substituent−substituent repulsion regulates the dye−dye intercation. Thus, *PSA* and, more in general, the electrostatic repulsion in between the dye molecules can be used to describe the dye−dye interaction and thereby the self-assembly scenario here: anisotropic nanoparticles are formed when the dye−dye electrostatic repulsion is lower and the interaction is strong, while weaker interaction yields isotropic nanoassemblies.

Lastly, the aspect ratio of the nanoparticles has been studied comparing it to the *PSA*. Results are reported in Figure 11b. It is evident that *PSA* controls the nanoparticle aspect ratio.[71] In particular, it decreases as the *PSA* increases. Again, if *PSA* is related to dye−dye interaction strength, it can be concluded that more anisotropic nanoparticles are formed when the dyes self-interact strongly, while weaker dye−dye interaction results in spherical assemblies. This relation of dye−dye interaction strength with supramolecular nanoparticle shape may be applied for other promising self-assembled systems such as in the case of aggregation-induced emission where subsituents control nanostructure and color.[68]

Strikingly, in the complex interplay of forces regulating electrostatic self-assembly, the *PSA* has a key role defining the shape of the nanoparticles. It summarizes the electrostatic repulsion of the interacting molecules and can be directly connected to the strength of the dye−dye interaction. Uncovering the role of the *PSA* as a molecular parameter controlling self-assembly is extremely promising and may be


DOI: 10.1021/jacs.5b11497
J. Am. Chem. Soc. 2016, 138, 1280−1293

used to predict the electrostatic self-assembly of a variety of kinds.

## CONCLUSIONS

In conclusion, we elucidated the nanoscale shape control in electrostatic self-assembly based on the role of molecular building blocks. The aspect ratio of the nanoparticles is related to the polyelectrolyte dendrimer generation and to the dye counterion structure. For instance, higher dendrimer generations produce more anisotropic nanoparticles. The dye valency is the key to the basic shape of the assemblies: divalent dyes form anisotropic nanoparticles, while trivalent dyes form spherical ones. Complementary, the loading ratio controls the number of dendrimers per aggregate and the dimensions of the nanoparticles. When the nanoassemblies have an anisotropic shape, it also regulates structural properties as the dimensions and the aspect ratio. On a molecular association level, a relation between the valency of the dye, the stacking angle, and the assembly shape has been established for the interaction with G4 dendrimer. For the trivalent dyes with different number of aromatic rings and different substituents the twist angle is constant. Divalent dyes, instead, stack with larger and varying angles.

Thermodynamic measurements have shown that the interaction of the building blocks is the crucial key to the definition of the nanoparticle shape. Considering the mutual interaction of the dyes, a threshold value of $\Delta H_{dye-dye}$ separating isotropic and anisotropic nanoaggregates has been found. This indicates that a certain value of enthalpy exchange is needed to obtain elongated nanoparticles. In more detail, a strong $\pi-\pi$ interaction leads to anisotropic structures. For the dye−polyelectrolyte interaction, a threshold value was detected as well.

We further examined which molecular parameters encode thermodynamics and thereby particle shape. Modeling molecular properties of the dye molecules has shown that electrostatic properties control the thermodynamics of the dye−dye interaction. In particular, the electrostatic potential at the molecular surface and the polar surface area determine the strength of the dye−dye interaction, which again controls the nanostructure of the polyelectrolyte−dye particles.

From these results, it will be possible to predict nanoparticle shapes knowing only the thermodynamic parameters for the interaction of the chosen molecular building blocks. Thus, a precise molecular design of the dye molecule (i.e., choosing appropriate substituents) will allow tailoring the structure of the nanoparticles. Hence, fundamental steps in developing a box of molecular "building bricks" allowing for a targeted structural design have been made. This may, for example, be of potential in the development of novel self-assembled photocatalysts or smart therapeutic carrier systems.

## EXPERIMENTAL SECTION

**Chemicals and Synthesis.** Poly(amidoamine) (PAMAM) dendrimer of different generations were obtained from Dendritech, Midland, MI, USA, and Sigma-Aldrich, Schnelldorf, Germany. The azo dyes Acid Red 26 (Ar26, C.I. 16150), Acid Red 27 (Ar27, C.I. 16185), and Acid Red 18 (Ar18, C.I. 16255) were obtained from Acros, Geel, Belgium. The azo dyes disodium 4-((4-*tert*-butylphenyl)-diazenyl)-3-hydroxynaphthalene-2,7-disulfonate (tBARAc), disodium 4-(phenyldiazenyl)-3-hydroxynaphthalene-2,7-disulfonate (ARAc), and trisodium 4-((4-sulfophenyl)diazenyl)-3-hydroxynaphthalene-2,7-disulfonate (SuARAc) were already synthesized and characterized in a previous study.[50] Disodium 4-((3-(hydroxymethyl)phenyl)diazenyl)-3-hydroxynaphthalene-2,7-disulfonate (ABnOHRAc), trisodium 4-((4-(carboxymethyl)phenyl)diazenyl)-3-hydroxynaphthalene-2,7-disulfonate (APhAcOHRAc), and disodium 5-((4-sulfophenyl)diazenyl)-8-aminonaphthalene-2-sulfonate (SuACAc) were newly synthesized by azo coupling according to the previously described procedure.[50] The precursors for synthesis were 4-aminophenylacetic acid (APhAcOH, Merck KGaA, Darmstadt, Germany), 3-aminobenzyl alcohol (ABnOH, Merck KGaA, Darmstadt, Germany), sulfanilic acid (SuA, Sigma-Aldrich, Schnelldorf, Germany), disodium 3-hydroxynaphthalene-2,7-disulfonate (R-Acid, RAc, Sigma-Aldrich, Schnelldorf, Germany), and 8-aminonaphthalene-2-sulfonic acid (1,7-Cleve's Acid, CAc, abcr, Karlsruhe, Germany). All azo dyes were purified as described previously[46] according to the literature.[72]

**Characterization of Azo Dyes.** Yields were calculated on the basis of carbon content from elemental analysis. NMR spectra showed that the product is salt free except for <1 wt % sodium acetate and a small amount of ethanol <1 wt % which could not be removed despite extended drying under high vacuum. The purities given below are corrected for residual amounts of sodium acetate and ethanol, which were determined by NMR. Azo dyes are known to possess multiple molecules of crystal water.[73] Thus, the pure dye contents are below 99%, which does not indicate impurities.

*Ar26.* $^1$H NMR ($D_2O$, 300 MHz, 25 °C), $\delta$ [ppm]: 7.62 (s, 1H); 7.52−7.40 (m, 2H); 7.38 (s, 1H); 6.53 (d, $J$ = 8.0 Hz, 1H); 5.95 (d, $J$ = 8.1 Hz, 1H); 5.35 (s, 1H); 1.44 (d, $J$ = 7.5 Hz, 6H). Anal. Calcd for $C_{18}H_{14}N_2Na_2O_7S_2$: C, 45.00. Found: C, 43.16. Dye content: 96%.

*Ar27.* $^1$H NMR ($D_2O$, 300 MHz, 25 °C), $\delta$ [ppm]: 8.05 (d, $J$ = 7.8 Hz, 1H); 8.01−7.93 (m, 2H); 7.87 (d, $J$ = 8.4 Hz, 1H); 7.75 (d, $J$ = 8.4 Hz, 1H); 7.68−7.50 (m, 2H); 7.16 (d, $J$ = 7.5 Hz, 1H); 7.11−6.91 (m, 2H). Anal. Calcd for $C_{20}H_{11}N_2Na_3O_{10}S_3$: C, 39.74. Found: C, 37.54. Dye content: 94%.

*Ar18.* $^1$H NMR ($D_2O$, 300 MHz, 25 °C), $\delta$ [ppm]: 8.96 (d, $J$ = 8.3 Hz, 1H); 8.76 (s, 1H); 8.55 (d, $J$ = 8.7 Hz, 1H); 8.30 (d, $J$ = 8.3 Hz, 1H); 7.91 (s, 1H); 7.70 (d, $J$ = 8.5 Hz, 1H); 7.50 (t, $J$ = 7.8 Hz, 1H); 7.40−7.24 (m, 2H); 6.33 (d, $J$ = 9.5 Hz, 1H). Anal. Calcd for $C_{20}H_{11}N_2Na_3O_{10}S_3$: C, 39.74. Found: C, 36.59. Dye content: 92%.

*ABnOHRAc.* $^1$H NMR ($D_2O$, 400 MHz, 20 °C), $\delta$ [ppm]: 7.95 (d, $J$ = 8.8 Hz, 1H); 7.71 (dd, $J$ = 8.6, 1.8 Hz, 1H); 7.64 (s, 1H); 7.40 (d, $J$ = 1.2 Hz, 1H); 7.00 (t, $J$ = 8.0 Hz, 1H); 6.92 (d, $J$ = 7.6 Hz, 1H); 6.87−6.85 (m, 2H); 4.35 (s, 2H). Anal. Calcd for $C_{17}H_{12}N_2Na_2O_8S_2$: C, 42.33. Found: C, 40.02. Dye content: 94%.

*APhAcOHRAc.* $^1$H NMR ($D_2O$, 400 MHz, 20 °C), $\delta$ [ppm]: 8.09 (d, $J$ = 8.8 Hz, 1H); 7.89 (s, 1H); 7.76 (dd, $J$ = 8.6, 1.8 Hz, 1H); 7.64 (d, $J$ = 1.2 Hz, 1H); 7.10 (d, $J$ = 8.4 Hz, 2H); 6.93 (d, $J$ = 8.4 Hz, 2H); 3.32 (s, 2H). Anal. Calcd for $C_{18}H_{11}N_2Na_3O_9S_2$: C, 40.61. Found: C, 37.16. Dye content: 91%.

*SuACAc.* $^1$H NMR ($D_2O$, 300 MHz, 25 °C), $\delta$ [ppm]: 8.11 (d, $J$ = 8.9 Hz, 1H); 7.92 (s, 1H); 7.67−7.54 (m, 3H); 7.13 (d, $J$ = 8.2 Hz, 2H); 7.04 (d, $J$ = 8.6 Hz, 1H); 6.24 (d, $J$ = 8.6 Hz, 1H). Anal. Calcd for $C_{16}H_{11}N_3Na_2O_6S_2$: C, 42.58. Found: C, 42.51. Dye content: 99%.

**Sample Preparation.** Stock solutions were prepared in Milli-Q water (>18.2 MΩ/cm) at pH = 10.5, where the PAMAM dendrimer is fully deprotonated. pH values were adjusted by adding NaOH or HCl standard solutions. All pH values were counter-checked by a freshly calibrated pH electrode. An aqueous solution of the dye at pH = 10.5 was diluted with Milli-Q water adjusted to pH = 10.5. Dendrimer stock solution at the same pH was added. After mixing, HCl was added at once under turbulent mixing to adjust the sample pH to 3.5, inducing assembly formation.

**Atomic Force Microscopy.** For AFM sample preparation, solutions with the same concentration as for light scattering were spin coated on freshly cleaved mica at 3000 rpm for 40 s (including 10 s acceleration time). AFM images were recorded in noncontact mode on a NanoSurf Easy Scan instrument (Boston, MA). For data processing the open access software Gwyddion was used.

**Light Scattering.** Measurements were carried out using an ALV 5000 correlator with 320 channels, a CGS 3 goniometer (ALV Langen, Germany), and a HeNe laser with a wavelength of $\lambda$ = 632.8 nm with 22 mW output power. A range of scattering angles of 30° < $\theta$ < 150° was covered. The instrument performs simultaneously static and dynamic


DOI: 10.1021/jacs.5b11497
J. Am. Chem. Soc. 2016, 138, 1280−1293

light scattering measurements. In this study, to extend the SANS spectrum at lower $q$, the static results have been used. This approach extends the curves in the $q$ range between $6.8 \times 10^{-4}$ and $2.5 \times 10^{-3}$ $nm^{-1}$. The data have been normalized to obtain the absolute intensity and then have been merged with the experimental data obtained by SANS. The standard concentration of PAMAM dendrimers was $c = 0.5$ g $L^{-1}$.

**Small Angle Neutron Scattering.** Samples for SANS were prepared in $D_2O$ with a dendrimer concentration of 0.5 and 0.2 g $L^{-1}$ for the samples not stable at the first concentration and transferred into quartz cells with 2 mm path length. Previous results on G4 nanoassemblies have shown no influence of the concentration on nanoparticle shape and a limited one on the dimensions. SANS studies were performed on D11 at the Institut Laue–Langevin, Grenoble, France, and on KWS2 at the Jülich Center for Neutron Scattering at the *Heinz Maier-Leibnitz Zentrum (MLZ)*, Munich, Germany. On D11 two different $\lambda$ were used: 6 and 13 Å. The first was used for 3 different sample–detector distances: 1.2, 8, and 39 m. The second was used only in the case of big nanoparticles at 39 m. The wavelength spread ($\Delta\lambda/\lambda$) was 0.09. A total scattering vector range of 0.007 $nm^{-1} < q < 5$ $nm^{-1}$ was investigated. At KWS2, a wavelength of 4.55 Å was used with 3 sample–detector distances: 2, 8, and 20 m. For some samples a different combination was used: 2, 4, and 20 m: the 8 m distance was replaced with 4 m to obtain a very similar scattering vector with a higher neutron flux. In this case a total scattering vector of 0.035 $nm^{-1} < q < 5$ $nm^{-1}$ was covered. Data were corrected for empty cell scattering, electronic background, and detector uniformity and then converted to absolute scale using secondary standards. Then the scattering of the solvent and the incoherent background was subtracted from the data. The scattering curve $I(q)$ was, where possible, analyzed by Guinier analysis followed by inverse Fourier transformation to obtain the pair distribution function $P(r)$ through the relationship

$$I(q) = 4\pi \int P(r) \frac{\sin(qr)}{qr} \mathrm{d}r \tag{5}$$

On the basis of the first results, structural modeling by standard fitting packages such as SASview was used to obtain the particle shape and dimensions.

For some samples the instrument resolution was taken into account in the fitting process to check its influence on the obtained results.

**UV–vis Spectroscopy.** Absorption spectra were recorded on a JASCO V-630 spectrometer using plastic cuvettes with 1 cm path length at dye concentrations of $c \approx 2 \times 10^{-5}$ mol $L^{-1}$. Once obtained, the experimental extinction coefficient has been fitted according to the relation

$$\varepsilon_D = \varepsilon_J \exp\left[-4 \ln 2 \frac{(\nu - \nu_J)^2}{\Delta\nu_{1/2,J}^2}\right] + \sum_{i=0}^{1} \varepsilon_i \exp\left[-4 \ln 2 \frac{(\nu - \nu_i)^2}{\Delta\nu_{1/2,i}^2}\right] \tag{6}$$

where $\varepsilon_D$ is the extinction coefficient of the dimer. This separation can be done because the spectral separation between the H and the J band is greater than the vibronic progression. The first term of the equation refers to the J band with $\varepsilon_J$ as extinction coefficient, $\nu_J$ as wavenumber, and $\Delta\nu_{1/2,J}$ as half-width of the Gaussian. The second term represents the H band extended to two vibronic transitions. From the fits, two different geometric parameters can be obtained according to the equation

$$\beta = 2 \arctan \sqrt{\frac{f_J}{f_H}} \tag{7}$$

$$R = \sqrt[3]{\frac{2.1410^7 \cos\beta}{\nu_M \Delta\nu_{H,J}}} \tag{8}$$

where $f_i$ is the oscillator strength for the $i$th band.

**Isothermal Titration Calorimetry.** ITC measurements were carried out with a MicroCal VP-ITC from Malavern Instrument Ltd., U.K. For the dye dilution experiments, one initial injection of 10 $\mu$L to saturate the titration cell wall was followed by 20 injections of 5 $\mu$L each. Dilution heats of PAMAM dendrimer were negligible in comparison to dye–dendrimer interaction energies. The time span between subsequent injections was 300 s. All experiments were conducted at 25 °C. For dye–dendrimer experiments 15–50 injections of 5–15 $\mu$L each were used. The time span between subsequent injections was 300 s. All experiments were conducted at 25 °C. Formic acid/formiate at pH = 4 was used as buffer system with $c$(buffer) = 15 mmol. Data analysis for dye–dendrimer experiments was performed using a one-site model as implemented in the MicroCal ITC data analysis software for Origin 7.0. The fit of the integrated heat per injection is performed according to a stepwise disaggregation model as described in ref 50. Errors on the free energy change $\Delta G$ are of the order of 2%, on the enthalpy change $\Delta H$ are of the order of 5%, while on entropy change $\Delta S$ are 15%.

**Molecular Modeling.** Calculations were carried out using the Spartan'14 software (Wave function Inc., Irvine, CA, USA, 2014). Molecular properties and electrostatic potential surfaces were generated with the density functional B3LYP level of theory using 6-31G* basis set in vacuum. All molecules were optimized for the equilibrium geometry with the maxima and minima in the electrostatic potential surface (0.002 electrons $au^{-3}$ isosurface) determined using a positive point charge in the vacuum as a probe. Here we might add that PSA has been calculated taking into account all the polar atoms in the molecule. This to highlight that we included also S into calculation that was not considered by the default program.

## AUTHOR INFORMATION


### Corresponding Author

*franziska.groehn@fau.de


### Notes

The authors declare no competing financial interest.

## ACKNOWLEDGMENTS

Major financial support of the projects involved by the German Science Foundation (DFG), the Interdisciplinary Center for Molecular Materials (ICMM, University Erlangen-Nürnberg) and the Institut Laue Langevin (ILL), Grenoble, France, is gratefully acknowledged. This work benefitted from SasView software, originally developed by the DANSE project under NSF award DMR-0520547. The study is based upon experiments performed at D11 at ILL, Grenoble, France, and at the KWS 2 instrument operated by JCNS at the Heinz Maier-Leibnitz Zentrum (MLZ), Garching, Germany. The authors also gratefully acknowledge the financial support provided by ILL, and by JCS to perform the neutron scattering measurements at ILL and at MLZ.

## REFERENCES


(1) Lehn, J. M. *Angew. Chem., Int. Ed. Engl.* **1988**, *27*, 89–112.
(2) Faul, C. F. J.; Antonietti, M. *Adv. Mater.* **2003**, *15*, 673–683.
(3) Pochan, D. J.; Chen, Z. Y.; Cui, H. G.; Hales, K.; Qi, K.; Wooley, K. L. *Science* **2004**, *306*, 94–97.
(4) Kaiser, T. E.; Wang, H.; Stepanenko, V.; Würthner, F. *Angew. Chem., Int. Ed.* **2007**, *46*, 5541–5544.
(5) Elmahdy, M. M.; Dou, X.; Mondeshki, M.; Floudas, G.; Butt, H. J.; Spiess, H. W.; Müllen, K. J. *J. Am. Chem. Soc.* **2008**, *130*, 5311–5319.
(6) Smulders, M. M. J.; Schenning, A. P. H. J.; Meijer, E. W. *J. Am. Chem. Soc.* **2008**, *130*, 606–611.
(7) Willerich, I.; Gröhn, F. *Angew. Chem., Int. Ed.* **2010**, *49*, 8104–8108.
(8) Mauro, M.; Aliprandi, A.; Cebrián Ávila, C.; Wang, D.; Kübel, C.; De Cola, L. *Chem. Commun.* **2014**, *50*, 7269–7272.




DOI: 10.1021/jacs.5b11497
*J. Am. Chem. Soc.* 2016, 138, 1280–1293

(9) Park, J. I.; Nguyen, T. D.; de Queirós Silveira, G.; Bahng, J. H.; Srivastava, S.; Zhao, G.; Sun, K.; Zhang, P.; Glotzer, S. C.; Kotov, N. A. *Nat. Commun.* **2014**, *5*, 3593−3598.
(10) Sijbesma, R. P.; Beijer, F. H.; Brunsveld, L.; Folmer, B. J. B.; Ky Hirschberg, J. H. K.; Lange, R. F. M.; Lowe, J. K. L.; Meijer, E. W. *Science* **1997**, *278*, 1601−1604.
(11) Beck, J. B.; Rowan, S. J. *J. Am. Chem. Soc.* **2003**, *125*, 13922−13923.
(12) Northrop, B. H.; Zheng, Y.-R.; Chi, K.-W.; Stang, P. *Acc. Chem. Res.* **2009**, *42*, 1554−1563.
(13) Gröger, G.; Meyer-Zaika, W.; Böttcher, C.; Gröhn, F.; Ruthard, C.; Schmuck, C. *J. Am. Chem. Soc.* **2011**, *133*, 8961−8971.
(14) Grimm, F.; Ulm, N.; Gröhn, F.; Düring, J.; Hirsch. *Chem. - Eur. J.* **2011**, *17*, 9478−9488.
(15) Faul, C. F. J.; Antonietti, M. *Chem. - Eur. J.* **2002**, *8*, 2764−2768.
(16) Zhang, Y.; Guan, Y.; Yang, S.; Xu, J.; Han, C. C. *Adv. Mater.* **2003**, *15*, 832−834.
(17) Xu, Y.; Bolisetty, S.; Ballauff, M.; Müller, A. H. E. *J. Am. Chem. Soc.* **2009**, *131*, 1640−1641.
(18) Yan, M.; Fresnais, J.; Berret, J.-F. *Soft Matter* **2010**, *6*, 1997−2005.
(19) Zhou, S.; Burger, C.; Chu, B.; Sawamura, M.; Nagahama, N.; Toganoh, M.; Hackler, U. E.; Isobe, H.; Nakamura, E. *Science* **2001**, *291*, 1944−1947.
(20) Discher, D. E.; Eisenberg, A. *Science* **2002**, *297*, 967−973.
(21) Nikolic, M. S.; Olsson, C.; Salcher, A.; Kornowski, A.; Rank, A.; Schubert, R.; Frömsdorf, A.; Weller, H.; Förster, S. *Angew. Chem., Int. Ed.* **2009**, *48*, 2752−2754.
(22) DeMuth, P. C.; Su, X.; Samuel, R. E.; Hammond, P. T.; Irvine, D. *Adv. Mater.* **2010**, *22*, 4851−4856.
(23) Gröhn, F.; Klein, K.; Koynov, K. *Macromol. Rapid Commun.* **2010**, *31*, 75−80.
(24) Guan, Y.; Antonietti, M.; Faul, C. F. J. *Langmuir* **2002**, *18*, 5939−5945.
(25) Glotzer, S. C. *Science* **2004**, *306*, 419−420.
(26) Glotzer, S. C.; Solomon, M. *Nat. Mater.* **2007**, *6*, 557−562.
(27) Palmer, L. C.; Velichko, Y. S.; Olvera de la Cruz, M.; Stupp, S. *Philos. Trans. R. Soc., A* **2007**, *365*, 1417−1433.
(28) Peterca, M.; Imam, M. R.; Leowanawat, P.; Rosen, B. M.; Wilson, D. A.; Wilson, C. J.; Zeng, X.; Ungar, G.; Heiney, P. A.; Percec, V. *J. Am. Chem. Soc.* **2010**, *132*, 11288−11305.
(29) Percec, V.; Sun, H.-J.; Leowanawat, P.; Peterca, M.; Graf, R.; Spiess, H. W.; Zeng, Z.; Ungar, G.; Heiney, P. A. *J. Am. Chem. Soc.* **2013**, *135*, 4129−4148.
(30) Douglas, J. F.; Dudowicz, J.; Freed, K. F. *Phys. Rev. Lett.* **2009**, *103*, 135701.
(31) Zhang, H.; Wang, D. *Angew. Chem.* **2008**, *120*, 4048−4051.
(32) Mahalik, J. P.; Muthukumar, M. *J. Chem. Phys.* **2012**, *136*, 135101.
(33) Camerel, F.; Faul, C. F. J. *Chem. Commun.* **2003**, 1958−1959.
(34) Gröhn, F.; Klein, K.; Brand, S. *Chem. - Eur. J.* **2008**, *14*, 6866−6869.
(35) Willerich, I.; Gröhn, F. *Chem. - Eur. J.* **2008**, *14*, 9112−9116.
(36) Li, Y.; Yildiz, U. H.; Müllen, K.; Gröhn, F. *Biomacromolecules* **2009**, *10*, 530−540.
(37) Ruthard, C.; Maskos, M.; Kolb, U.; Gröhn, F. *Macromolecules* **2009**, *42*, 830−840.
(38) Gröhn, F. *Soft Matter* **2010**, *6*, 4296−4302.
(39) Willerich, I.; Ritter, H.; Gröhn, F. *J. Phys. Chem. B* **2009**, *113*, 3339−3354.
(40) Willerich, I.; Li, Y.; Gröhn, F. *J. Phys. Chem. B* **2010**, *114*, 15466−15476.
(41) Willerich, I.; Gröhn, F. *Macromolecules* **2011**, *44*, 4452.
(42) Ruthard, C.; Schmidt, M.; Gröhn, F. *Macromol. Rapid Commun.* **2011**, *32*, 706−711.
(43) Düring, J.; Hölzer, A.; Kolb, U.; Branscheid, R.; Gröhn, F. *Angew. Chem., Int. Ed.* **2013**, *52*, 8742−8745.
(44) Frühbeißer, S.; Gröhn, F. *J. Am. Chem. Soc.* **2012**, *134*, 14267−14270.
(45) Willerich, I.; Schindler, T.; Ritter, H.; Gröhn, F. *J. Phys. Chem. B* **2011**, *115*, 9710−9719.
(46) Willerich, I.; Gröhn, F. *J. Am. Chem. Soc.* **2011**, *133*, 20341−20356.
(47) Jansen, J. F. G. A.; de Brabander-van den Berg, E. M. M.; Meijer, E. *Science* **1994**, *266*, 1226−1229.
(48) Richter-Egger, D. L.; Landry, J. C.; Tesfai, A.; Tucker, S. A. *J. Phys. Chem. A* **2001**, *105*, 6826−6833.
(49) Neumann, B.; Huber, K.; Pollmann, P. *Phys. Chem. Chem. Phys.* **2000**, *2*, 3687−3695.
(50) McRae, E. G. *Aust. J. Chem.* **1961**, *14*, 329.
(51) McRae, E. G. *Aust. J. Chem.* **1961**, *14*, 344.
(52) McRae, E. G. *Aust. J. Chem.* **1961**, *14*, 354.
(53) Kasha, M.; Rawls, H. R.; Ashraf El-Bayoumi. *Pure Appl. Chem.* **1965**, *11*, 371.
(54) Monahan, A. R.; Blossey, D. F. *J. Phys. Chem.* **1970**, *74*, 4014.
(55) The resulting interdye distances, as compared to X-ray data from the literature,[58] seems to be too large as values between 0.3 and 0.4 nm were found in the literature. This difference is due to the approximation done using the exciton theory where the interacting dye molecules are described as point dipole.
(56) It must be said that this approach is formally incorrect: describing a cooperative binding with a one-site model is simplifying the process. However this approach is reasonable to obtain reliable results.[61]
(57) Bhadra, K.; Maiti, M.; Kumar, G. S. *Biochim. Biophys. Acta, Gen. Subj.* **2008**, *1780*, 1054−1061.
(58) Hunter, C. A.; Sanders, J. K. M. *J. Am. Chem. Soc.* **1990**, *112*, 5525−5534.
(59) Sinnokrot, M. O.; Sherrill, C. D. *J. Phys. Chem. A* **2003**, *107*, 8377−8379.
(60) Wheeler, S.; Houk, K. *J. Am. Chem. Soc.* **2008**, *130*, 10854−10855.
(61) Martinez, C. R.; Iverson, B. L. *Chem. Sci.* **2012**, *3*, 2191−2201.
(62) Wheeler, S. *J. Am. Chem. Soc.* **2011**, *133*, 10262.
(63) Cockroft, S. L.; Perkins, J.; Zonta, C.; Adams, H.; Spey, S. E.; Low, C. M. R.; Vinter, J. G.; Lawson, K. R.; Urch, C. J.; Hunter, C. A. *Org. Biomol. Chem.* **2007**, *5*, 1062−1080.
(64) Rashkin, M. J.; Waters, M. L. *J. Am. Chem. Soc.* **2002**, *124*, 1860−1861.
(65) Kelder, J.; Grootenhuis, P. D.; Bayada, D. M.; Delbressine, L. P.; Ploemen, J. P. *Pharm. Res.* **1999**, *16*, 1514−9.
(66) Ertl, P.; Rohde, B.; Selzer, P. *J. Med. Chem.* **2000**, *43*, 3714−3717.
(67) Wüthner, F.; Yao, S.; Debraedemaecker, T.; Wortmann, R. *J. Am. Chem. Soc.* **2002**, *124*, 9431−9447.
(68) Niu, C.; Zhao, L.; Fang, T.; Deng, X.; Ma, H.; Zhang, J.; Na, N.; Han, J.; Ouyang, J. *Langmuir* **2014**, *30*, 2351−2359.
(69) Chen, Z.; Lohr, A.; Saha-Möller, C. R.; Würthner, F. *Chem. Soc. Rev.* **2009**, *38*, 564−584.
(70) Su, W.; Zhang, Z.; Zhao, C.; Li, X.; Jiang, J. *ChemPhysChem* **2007**, *8*, 1857−1862.
(71) To calculate the aspect ratio of the nanoassemblies formed by ABnOHRAc and G4 dendrimer, the Kuhn length has been used instead of the total length. If the total length is used the aspect ratio is large and cannot be related to the *PSA* while the aspect ratio of the subunits does.
(72) Robinson, C.; Mills, H. A. T. *Proc. R. Soc. London, Ser. A* **1931**, *131*, 576−595.
(73) Kratky, O.; Pilz, I.; Ledwinka, H. *Monatsh. Chem.* **1967**, *98*, 227−230.


DOI: 10.1021/jacs.5b11497
*J. Am. Chem. Soc.* 2016, 138, 1280−1293